https://doi.org/10.5194/tc-2019-175
Preprint. Discussion started: 4 September 2019

The Cryosphere
Discussions
Open Access

# Use of Sentinel-1 radar observations to evaluate snowmelt dynamics in alpine regions

Carlo Marin[1], Giacomo Bertoldi[2], Valentina Premier[1], Mattia Callegari[1], Christian Brida[2], Kerstin Hürkamp[3], Jochen Tschiersch[3], Marc Zebisch[1], and Claudia Notarnicola[1]

[1]Institute for Earth Observation, Eurac Research, Viale Druso, 1 I-39100 Bolzano, Italy
[2]Institute for Alpine Environment, Eurac Research, Viale Druso, 1 I-39100 Bolzano, Italy
[3]Helmholtz Zentrum München, German Research Center for Environmental Health, Institute of Radiation Medicine, Ingolstädter Landstraße 1, 85764 Neuherberg, Germany

**Correspondence:** Carlo Marin (carlo.marin@eurac.edu)

**Abstract.** Knowing the timing and the evolution of the snow melting process is very important, since it allows the prediction of: i) the snow melt onset; ii) the snow gliding and wet-snow avalanches; iii) the release of snow contaminants and iv) the runoff onset. The snowmelt can be monitored by jointly measuring snowpack parameters such as the snow water equivalent (SWE) or the amount of free liquid water content (LWC). However, continuous measurements of SWE and LWC are rare and difficult to be obtained. On the other hand, active microwave sensors such as the Synthetic Aperture Radar (SAR) mounted on board of satellites, are highly sensitive to LWC of the snowpack and can provide spatially distributed information with a high resolution. Moreover, with the introduction of Sentinel-1, SAR images are regularly acquired every 6 days over several places in the world. In this paper we analyze the correlation between the multi-temporal SAR backscattering and the snowmelt dynamics. We compared Sentinel-1 backscattering with snow properties derived from in situ observations and process-based snow modeling simulations for five alpine test sites in Italy, Germany and Switzerland considering two hydrological years. We found that the multi-temporal SAR measurements allow the identification of the three melting phases that characterize the melting process i.e., moistening, ripening and runoff. In detail, we found that the C-band SAR backscattering decreases as soon as the snow starts containing water, and that the backscattering increases as soon as SWE starts decreasing, which corresponds to the release of meltwater from the snowpack. We discuss the possible reasons of this increase, which are not directly correlated to the SWE decrease, but to the different snow conditions, which change the backscattering mechanisms. Finally, we show a spatially-distributed application of the identification of the runoff onset from SAR images for a mountain catchment, i.e., the Zugspitze catchment in Germany. Results allow to better understand the spatial and temporal evolution of melting dynamics in mountain regions. The presented investigation could have relevant applications for monitoring and predicting the snowmelt progress over large regions.

## 1 Introduction

Seasonal snowpack is one of the most important water resources present in nature. It stores water during the winter and releases it in spring during the melting. In mountain regions, snow storage is essential for the freshwater supply of the lowlands, making

https://doi.org/10.5194/tc-2019-175
Preprint. Discussion started: 4 September 2019

the mountains the water towers of the downstream regions (Viviroli and Weingartner, 2004). In fact, the temporally delayed release of the water from the head-watersheds to the forelands is essential for a large number of human activities such as agriculture irrigation, drinking water supply and hydropower production (Beniston et al., 2018). In particular, in the Alps, discharges in May and June are largely dictated by snowmelt, while from July to September are influenced by glacier melt (Wehren et al., 2010) and liquid precipitation. On the other hand, wet snow may contribute to natural disasters such as wet snow avalanches (Bellaire et al., 2017) or wet-snow gliding (Fromm et al., 2018). Moreover, in case of accumulated contaminant release from a snowpack, initial runoff meltwater can be highly enriched and is able to cause severe impact on the water quality (Hürkamp et al., 2017). Precise predictions of the timing of first runoff will therefore enable countermeasures or the estimation of the scope of action. In this context, knowing the temporal and spatial evolution of the snow melting process is very important for a proactive management of the water resources and for hazard mitigation.

The melt period can be generally separated in three phases (Dingman, 2015): i) moistening, ii) ripening and iii) runoff. The moistening is the initial phase of the snowmelt. The air temperature and solar radiation increase and due to heat exchanges and/or rain the superficial layers of the snowpack start melting. The ripening phase begins when the maximum retention capacity of the pores is exceeded. The wetting front penetrates through the snowpack, favored by repeated cycles of melting and refreezing, but the meltwater is not yet released. During this phase, the snowpack becomes isothermal and when no more liquid water can be retained, the runoff phase starts. The snowmelt process is a non-linear process affected by the strong variability of both the snowpack characteristics and the meteorological forcings that affect the snow. In order to obtain useful information about the progression of the melting process, non-invasive techniques that allow performing multiple measurements at the same location should be exploited. For this purpose, measurements of meteorological variables such as air temperature, snow temperature, relative humidity, wind speed, precipitation, and solar radiation are usually employed to extract information on snow melt dynamics (Kinar and Pomeroy, 2015). However, the most significant state variables to properly identify the three melting phases are the snow water equivalent (SWE), i.e. the total mass of liquid and solid water stored in form of snow, and the liquid water content (LWC), i.e. the mass of liquid water inside the snowpack. An increase of LWC in time indicates a moistening process going on, following the downward penetrating water front, that brings the snowpack to first a partial and later a complete isothermal state, which corresponds to the generation of water runoff, which corresponds to a significant decrease of SWE.

Continuously measure SWE and LWC is therefore essential to monitor the snowpack melting dynamics. So far, the most common method to manually measure SWE is using snow sampling tubes, while the most spread techniques for automatic SWE measurement include snow pillows and snow scales (Kinar and Pomeroy, 2015). The establishing and the maintenance of these kinds of measurements are very costly and a relatively limited number of continuous measurements of SWE are available in the Alps. Direct measurements of LWC are usually performed through empirical estimations (e.g. the hand test), or indirect assessments based on snow temperature. Recently, some promising systems that exploit the dielectric properties of the snow in the microwave region of the electromagnetic (EM) spectrum have been presented to allow a continuous and nondestructive measuring of LWC. In particular, three systems have demonstrated to be effective and robust in operational conditions: i) the snowpack analyzer (SPA) (Stähli et al., 2004); ii) the snow sense (Koch et al., 2014) based on GPS signals;

and iii) the upward-looking Ground Penetrating Radar (upGPR) (Schmid et al., 2014). All of them are commercial systems buried under the snowpack and rely on different methods for the dielectric constant estimation. Interestingly, these EM devices can be used to measure the SWE as well. However, all these ground-based measurements are limited in application to a single point, require calibration to relate the dielectric constant to volumetric snow LWC, and some of them are expensive, power intensive and laborious to be installed and maintained. These limitations complicate the possibility to monitor and understand the meltwater runoff and the snow stability considering also the spatial variability of the snowmelt dynamics.

To mitigate these limitations, energy based, multilayer physically based snow models can simulate SWE and LWC at high spatial and temporal resolution (Essery et al., 2013). Such kind of models account for shading, shortwave and longwave radiation, and turbulent fluxes of sensible and latent heat (Mott et al., 2011), but can differ in the way they parametrize snow metamorphism, grain size evolution, snow layering and liquid water percolation (Wever et al., 2014). They can range from very detailed approaches with a Lagrangian representation of snow layers as avalanche-forecasting models like CROCUS (Brun et al., 1992) or SNOWPACK/ALPINE3D (Bartelt and Lehning, 2002; Lehning et al., 2006) to more simplified approaches as the ones of hydrologically-oriented Eulerian models as AMUNDSEN (Strasser et al., 2011) or GEOtop (Endrizzi et al., 2014). Therefore, snow models can provide detailed information about the snow properties starting from observed meteorological conditions, which can be reliably acquired especially at plot-scale. However, model performances are affected by uncertainties and errors related to model structure (Avanzi et al., 2016), meteorological forcing (Raleigh et al., 2015) and model parametrizations (Engel et al., 2017; Günther et al., 2019). Therefore, there is the need of snow observations with high temporal and spatial resolution, distributed over a large area and systematically acquired.

In the past years, Synthetic Aperture Radar (SAR) has demonstrated to be a valid tool to identify the wet snow i.e., snow that contains a given amount of free liquid water (Nagler and Rott, 2000; Dong, 2018). In fact, SAR measurements are highly sensitive to the liquid water in the snowpack and the increase of the LWC causes a high dielectric loss that increases the absorption coefficient generating backscattered signal with low intensity (Ulaby et al., 2015). This physical principle has been exploited for the generation of wet snow maps by the bi-temporal algorithm proposed by (Nagler and Rott, 2000) and further improved in (Nagler et al., 2016). However, the increase of the liquid water content explains only partially the decrease of the backscattering coefficient. Indeed, as pointed out in Shi and Dozier (1995) and Baghdadi et al. (2000), the relationship between the coefficient of backscattering and the snow wetness can cause an increment of the backscattering value depending on the conditions of the snow roughness, snow density, snow layering, snow grain size and local incidence angle. This large number of unknowns, upon which the SAR backscattering is dependent on, defines a complex multiparametric problem that is difficult or even impossible to solve without introducing some simplification assumptions. So, even though some works have been presented that try to extract the LWC using C-band SAR images (Shi and Dozier, 1995; Longepe et al., 2009), at the best of our knowledge there are no attempts to use the SAR as source of information for describing the multi-temporal evolution of the snow melting process. Progress has been hampered by: i) the lack of ground truth information; ii) the relative high number of sources of uncertainty of the SAR signal; and iii) the difficulty to access SAR data in the past. This has changed since 2014 with the introduction of the Sentinel-1 (S-1) mission from the European Space Agency (ESA) and the European Commission (EC) guarantying the availability of C-band SAR images free of charge. In detail, S-1 is a constellation made up

https://doi.org/10.5194/tc-2019-175
Preprint. Discussion started: 4 September 2019

of two near-polar sun-synchronous satellites that acquire images early in the morning and late in the afternoon, with a nominal resolution of 20 m and a revisit time of 6 days. Moreover, as discussed before, an increasing number of data on relevant snow parameters related to the snowmelt are collected by operational systems (e.g. by SPA) or derived by physically based snow models. The information on SWE and LWC provided by independent sources opens new opportunities for better understanding the relationship between the snowpack properties during the melting phase and the multi-temporal SAR backscattering.

The aim of this work is to evaluate the information that S-1 can provide on the monitoring of the snowmelt dynamics. In particular, we provide the theoretical EM background for understanding the impact on the multi-temporal SAR backscattering of a melting snowpack. Then, we analyze the relationship between the multi-temporal SAR signal acquired from S-1 and in situ measurements of LWC and SWE in the Alps. Given the limited number of point-related continuous SWE and LWC measurements available in the test area, we made use of the physically based model SNOWPACK to simulate the snow properties in other locations where only meteorological data and snow depth were available. This allowed us to define five test sites at different altitudes in the Alps, where the interactions of S-1 backscattering with the snowpack were studied in detail during two melting seasons. On the basis of the outcomes of the study, we propose an interpretation scheme to be applied to multi-temporal dual polarimetric C-band SAR data in order to identify the different snow melting phases of moistening, ripening and runoff. Finally, we demonstrate the effectiveness of the proposed approach in a real application scenario to provide a spatially distributed information about the melting phases of the snowpack in alpine terrain, which can be used for monitoring and predicting the snowmelt progress over large regions.

## 2 Background

In this section we report the theoretical background on which this work is based on. First, the snow melting process is explained from a physical point of view and the different phases are identified considering the information of LWC and SWE. Then, the response of the SAR backscattering to the wet snow is described in detail.

### 2.1 Snow melting process

Figure 1 illustrates the snow cover development during the melting season considering the snow status in the morning and in the afternoon, when the S-1 descending and ascending data is acquired respectively. Hypothetical values of LWC and SWE are reported on the right side of the figure. In general, the liquid water is introduced in the snow by rain and/or melt due to heat exchange and the incoming flux of shortwave radiation flux, which varies with slope, aspect and elevation. In both cases, the snowpack starts melting at the surface (Techel and Pielmeier, 2011). This superficial moistening phase can be identified by comparing observations from the coldest and warmest period of the day i.e., a diurnal cycle is visible. Interestingly, the SAR acquisitions are approximately acquired around these two periods. The liquid water released or absorbed from the superficial layers gets in contact with the subfreezing snow present underneath and freezes. This releases latent heat that causes the snowpack to warm up starting the process of snow ripening. Repeated cycles of partial melting during the day and refreezing during the night induce the development of the wetting front into the snow. This is generally not uniform, since infiltrations usually start through isolated "flow fingers" which enlarge into meltwater channels due to the passing of time. Therefore, the ripening of the snowpack may be different year by year or considering different areas. In fact, climatic factors or snowpack stratifications may induce different behaviors. At the point of full water saturation, the snow layer cannot retain any more liquid water. Further absorption of energy produces water output, which, depending on soil properties, ice and water content, could infiltrate in the soil or appear as surface runoff (DeWalle and Rango, 2008). The runoff phase is characterized by a significant decrease of SWE.

During the melting, the presence of liquid water inside the snowpack directly affects the grain size, the grain shape and the density of the pack (Pomeroy and Brun, 2001). Indeed, during the melt process the snow undergoes to a rapid metamorphism that leads to a growing and a rounding of the grains linked to an increase of the snow density. Moreover, it is important to underline that during the melt season a general increase of the roughness of the snow surface is observed (Fassnacht et al., 2009) due to localized melting pattern (i.e., flow fingers) and rain on snow events.

## 2.2 SAR backscattering response to wet snow

From an EM point of view, the snowpack is an inhomogeneous medium composed of scattering elements with different sizes, shapes, orientations and permittivity values. The backscattering $\sigma^0$ produced by an EM wave generated by SAR over such a medium can be modeled as an incoherent sum of three contributions (Shi and Dozier, 1995; Ulaby et al., 2015): the surface scattering produced at the air-snow interface, $\sigma^0_{sup}$, the surface scattering produced at the snow-ground interface attenuated by the snowpack, $\sigma^0_{grd}$, and the volumetric scattering of the snowpack, $\sigma^0_{vol}$. The intensity of these contributions depends on parameters related to: i) the sensors i.e., frequency, local incidence angle (LIA) and polarization; ii) the snowpack properties i.e., liquid water content (LWC), density (DS), ice particle size and shape (GS), surface roughness (RS), which is usually described by the standard deviation of the height and the correlation length of the surface; and iii) the ground proprieties. In this paper we focus on the use of the C-band SAR mounted on board of S-1, and therefore all the parameters related to the sensor are known. Nonetheless, deriving the theoretical behavior of the time series of $\sigma^0$ for a given LIA for one hydrological year is complex. Indeed, the relationship between the backscattering and the snow parameters forms a non-linear system of equations. In the following we identify the main scattering mechanisms isolating the contribution of each parameter to the total backscattering.

During the accumulation period, dry snow is almost transparent for C-band, and the radar echo can penetrate the snow for several meters. In this situation, the main scattering source is the snow-ground interface (see Fig. 2) and the backscattering is almost insensitive to different snow parameters (Rott and Mätzler, 1987; Shi and Dozier, 1993). During the melting period, the increase of the free liquid water inside the snowpack causes high dielectric losses, which increase the absorption coefficient. By considering a sufficiently thick snowpack, this leads to a rapid decrease of $\sigma^0_{grd}$, which can be then neglected. By assuming constant all the parameters but the LWC, the increase of LWC causes the volume scattering to decrease and the backscattering becomes sensitive to surface roughness (Shi and Dozier, 1995). When the surface is smooth e.g., according to the Frauenhofer criterion (Ulaby et al., 2015), volume scattering dominates and therefore the increase of LWC results in a decrease of the total backscattering. Whereas, when the surface is rough the surface scattering dominates, thus with the increase of LWC the total backscattering tends to increase. The amount of wetness from which the surface scattering becomes predominant depends mainly on the surface roughness and LIA and may vary from about 1% to 6% of the total volume (Magagi and Bernier, 2003). However, other parameters play a role in this mechanism: by assuming constant all the parameters but the snow density, the volume scattering decreases at the increase of the snow density, if all the other parameters are kept fixed. Vice versa, the grain size increases the volume scattering. It is finally worth stressing the fact that the response to the wet snow becomes more complex in case of the snowpack in forest (Koskinen et al., 2010). In this case the total backscattering $\sigma^0$ is a function also of the forest stem volume. This can be estimated and taken into account, nonetheless in this work we focus on the identification of snow melting phase in open areas.

The main scattering mechanisms and their influence on the backscattering are reported in Table 1. Even though the table is reporting all the backscattering mechanisms of the different snow conditions during the melting process, the multi-temporal behavior that characterizes the three phases of moistening, ripening and runoff has not yet been studied in the past and remains mainly unsolved. Indeed, as described in the previous section, as soon as the LWC increases, the snowpack undergoes the wet-snow metamorphism that increases the density and the snow grain size, round the grains and induces an increase on the superficial roughness. In the following we will consider the real time series of backscattering recorded by S-1 during two hydrological years in the proximity of five test sites where LWC and SWE were measured or simulated. The outcome of this study will be exploited to: i) understand if a characteristic relation can be recognized from the comparison between the multi-temporal SAR signal and the melting phases; and ii) define some rules to automatically identify the beginning of each melting phase from the time series of $\sigma^0$.

## 3 Dataset description

In this section, we present the experimental sites and we describe the collected in situ data, the SNOWPACK set up and S-1 data.

### 3.1 Test sites description, and in situ data

For ground truth and as input for the simulations with SNOWPACK, we consider five snow and meteorological weather stations with different location in terms of place and altitude in the European Alps, equipped with different installed sensors. Among these, one is located in Bavaria (Germany), three in South Tyrol (Italy) and one in Graubünden (Switzerland). In detail, considered parameters are wind velocity (VW), wind direction (DW), air temperature (TA), relative humidity (RH), snow depth (HS), snow temperature at different depths (TS), surface temperature (TSS), soil temperature (TSG), incoming shortwave radiation (ISWR), incoming longwave radiation (ILWR), outgoing shortwave radiation (OSWR), snow water equivalent (SWE), snow density (DS), liquid water content (LWC) and ice content (IC). The considered data records started from the 1st October 2016 in order to cover the two winter seasons 2016/2017 and 2017/2018. An overview of the location of the stations is presented in Figure 3 and a summary with the available parameters is presented in Table 2.

#### 3.1.1 Zugspitze (Werdenfelser Alps, Germany)

The station is located in the Northern Calcareous Werdenfelser Alps, being part of the Zugspitze massif. It is part of the snow monitoring stations network of the Bavarian Avalanche Warning Service (Lawinenwarnzentrale Bayern) and located on a flat plateau at the southern slope of Mt. Zugspitze summit (2962 $\mathrm{m}$ a.s.l.), the so-called Zugspitzplatt (1500-2700 $\mathrm{m}$ a.s.l.), which is surrounded by several summits in the north, south and west and drained by the Partnach River to the east. Beside a standard meteorological station, the site is additionally equipped with a snow scale and a snow pack analyzer (SPA) to record SWE, DS, LWC and IC. The SPA uses a time-domain reflectometry (TDR) at high frequencies and a low-frequency impedance analyzer. By exploiting different frequencies, the SPA is able to determine the volumetric ice, air and water content as well as the density by measurement of the complex impedance of the snow layer. The EM pulse propagates along three 5 $\mathrm{m}$ long sensor bands, horizontally installed in 10 $\mathrm{cm}$, 30 $\mathrm{cm}$ and 50 $\mathrm{cm}$ above ground in 2016/2017. In 2017/2018 the heights of the bands were changed to 10 $\mathrm{cm}$, 20 $\mathrm{cm}$ and 30 $\mathrm{cm}$ due to a frequent failure of the uppermost sensor in the preceding years. This allows the measurement of the bulk properties of the snowpack rather than a point measurement as well as a tracking of the downward penetrating water front inside the snowpack. Combined with information on the snow height bulk, LWC is determined. The SPA has not been calibrated for the test site, but it is used with standard set-up parameters and an internal calibration by the manufacturer. This results in unreliable LWC values of about 2-3 $\%$ when the snowpack is dry. Moreover, given that no bulk information of LWC for the total thickness of the snowpack is provided by the SPA, we did not use the SPA LWC in this study. Snow height is recorded by an ultrasound sensor, installed at 6 $\mathrm{m}$ height. The sensors for the meteorological parameters are installed at a crossbar of the 6 $\mathrm{m}$ mast, too, besides the wind sensor, which is at 6.5 $\mathrm{m}$ height. The maximum snow height was 3.3 $\mathrm{m}$ during winter 2016/2017 and 3.9 $\mathrm{m}$ in January 2018. The area is continuously covered by snow between December and May each year. During the accumulation period, the stations records showed that no significant snowmelt runoff at the snow base occurred at any time since 2012 (Hürkamp et al., 2019). During the observed winter seasons the mean monthly wind velocity exceeded 3 $\mathrm{ms}^{-1}$ in the winter months, therefore wind drift could likely alter snow accumulation. The amount of mean annual precipitation is 2000 $\mathrm{mm}$.

#### 3.1.2 Alpe del Tumulo (South Tyrol, Italy)

The station is located on an alpine pasture in the North of Val Passiria. For this and the other South Tyrolean stations, the temperature sensor is installed at a 2.8 $\mathrm{m}$ height and the wind sensor at 5.5 $\mathrm{m}$. The site is weakly windy, with mean monthly velocity usually around 2 $\mathrm{ms}^{-1}$. The maximum snow height was around 1.5 $\mathrm{m}$ during winter 2016/2017 and around 2 $\mathrm{m}$ during the winter 2017/2018. No continuous measurements of LWC and SWE are available for this and the other South Tyrolean stations.

### 3.1.3 Clozner Loch (South Tyrol, Italy)

The station is located in Lauregno (Alta Val di Non) on an almost flat site. The mean monthly wind velocity seldom exceeds 2 $\mathrm{ms}^{-1}$. The snow height never exceeded 1 $\mathrm{m}$ during the winter 2016/2017 and the maximum height reached during the winter 2017/2018 was around 1.5 $\mathrm{m}$.

### 3.1.4 Malga Fadner (South Tyrol, Italy)

The station is located on an alpine pasture in Valle Aurina. The mean monthly wind velocity never exceeds 2 $\mathrm{ms}^{-1}$. The maximum snow height was less than 1.5 $\mathrm{m}$ during winter 2016/2017 and around 2 $\mathrm{m}$ during the winter 2017/2018.

### 3.1.5 Weissfluhjoch (Graubünden, Switzerland)

The automatic weather station is located at Weissfluhjoch, Davos, Switzerland. It is mantained by the WSL Institute for Snow and Avalanche Research SLF. The data are regulary updated and made freely available (WSL Institute for Snow and Avalanche Research SLF, 2015). The wind sensor is intalled at 5.5 $\mathrm{m}$ and the temperature sensor at 4.5 $\mathrm{m}$. The site is quite windy, with mean monthly velocity usually around 2 $\mathrm{ms}^{-1}$ or sometimes greater than this value. The maximum snow height was around 2 $\mathrm{m}$ during winter 2016/2017 and around 3 $\mathrm{m}$ during the winter 2017/2018. In this study, SWE GPS-derived measurements are used (Koch et al., 2019), which are also freely made available upon request.

## 3.2 SNOWPACK model set up

As described in the introduction, the proper identification of the melting phases requires a precise knowledge of the evolution of LWC and SWE. However, these parameters are not always available for the selected test sites. For this reason, there is the need to set up snowpack simulations for obtaining the missing parameters. In this work we used the physically-based model SNOWPACK, a one-dimensional (1-D) model developed by the WSL Institute for Snow and Avalanche Research, SLF (Bartelt and Lehning, 2002). The model solves 1-D partial differential equations governing the mass, energy and momentum conservation. Heat transfer, water transport, vapor diffusion and mechanical deformation of a phase changing snowpack are modeled assuming snow as a three-component (ice, water and air) porous material. Meteorological data are used as input for the model. Required parameters are air temperature, relative humidity, wind velocity, incoming longwave radiation and/or outgoing shortwave radiation, incoming longwave radiation and/or surface temperature, precipitation and/or snow depth and soil temperature. The data were taken or derived from the in situ measurements at the test sites. Meteo-IO (Bavay and Egger, 2014) is used as pre-processing tool to check erroneous data, fill the gaps and generate missing parameters. In the current case, the ground temperature is generated as a constant value assumed to be equal to the melting temperature if missing, and the incoming longwave radiation is calculated through an all-sky parametrization, which makes use of air temperature and humidity (Unsworth and Monteith, 1975; Dilley and O'brien, 1998). Fresh snowfall must be provided as initial condition. Since direct snow precipitation measurements are not available, the amount of new snow is forced by subtracting the model snow depth to the measured snow depth. This difference is assumed to be fresh snow only if reliable humidity and temperature conditions

https://doi.org/10.5194/tc-2019-175
Preprint. Discussion started: 4 September 2019

are verified, using the approach proposed and validated by (Mair et al., 2016) and implemented in the SNWOPACK model. This approach has been validated against snow pillow observations and resulted more reliable compared to heated tipping bucked rain gauges, which may underestimate solid precipitation up to 40% (Sevruk et al., 2009). The energy exchanges on the snowpack surface are imposed either using a Neumann boundary condition (BC), i.e. the energy fluxes are forced, or a Dirichlet BC, i.e. imposing the surface temperature except during ablation when again a Neumann BC is imposed. Additionally, a Dirichlet BC is imposed at the ground interface. A neutral atmospheric surface layer using the Monin – Obukhov similarity theory is imposed. The used water transport model is the NIED scheme proposed by Hirashima et al. (2010). A typical time step of 15 minutes is used for the simulations.

Since the SNOWPACK simulations are used in this work as reference data to be compared against the SAR backscattering, we calibrated the model considering the best agreement in the analyzed years 2016-2018 with in situ snow depth, snow temperatures at three different depth TS1 (0 $\mathrm{m}$ from the ground), TS2 (0.2 $\mathrm{m}$ from the ground) and TS3 (0.5 $\mathrm{m}$ from the ground) and SWE, when available. Pearson correlation coefficient ($\rho$) and the mean absolute error (MAE) have been computed for these variables. Roughness is used as calibration parameter. The results are reported in Table 3.

### 3.3 Remote sensing observations

S-1 is a two satellites constellation with a revisit time of 6 days with the same acquisition geometry and able to acquire dual polarimetric C-band (central frequency of 5.405 GHz) SAR images with a nominal resolution of $2.7 \times 22$ $\mathrm{m}$ to $3.5 \times 22\mathrm{m}$ in Interferometric Wide swath mode (IW). S-1 works in a pre-programmed way in order to build a consistent long-term data archive of images all around the world. IW acquisitions have a swath of about 250 km. This, together with the cycle length of the satellites of 175 orbits, allows the acquisition of more tracks over a given location at the middle latitudes such as the Alps. Therefore, in 6 days more than one acquisition may be available for the area of interest. Table 4 indicates the most relevant parameters related to the data acquisition for each of the selected locations. For the five test sites a total of about 1300 acquisitions were considered. The data used for the presented study are Level-1 ground range detected data, consisting of focused SAR data that have been detected, multi-looked and projected to ground range using an earth ellipsoid model by the data provider. The resulting products have approximately square spatial spacing of 10 by 10 meters. Phase information is lost for this data. This data can be downloaded free of charge form the Copernicus data hub (https://scihub.copernicus.eu/). In order to correct the complex topographic terrain, typical of mountain regions, and to reduce the speckle noise that affects SAR acquisitions, a tailored pre-processing has been applied for all the analyzed data. In detail, the pre-processing operations are performed using the tools included in SNAP (Sentinel Application Platform) version 6.0 and some custom tools developed in Python. In detail, the S-1 backscatter pre-processing operations are the following (S indicates SNAP tool, C indicates custom tool): 1) application of the precise Sentinel orbit to the data (S); 2) removal of the thermal noise present in the images (S); 3) temoval of the noise present at the border of the images (C); 4) beta nought calibration (S); 5) assembly of the S-1-tiles coming from the same track (S); 6) co-registration of the multi-temporal images (S); 7) multi-temporal filtering with a window size 11x11 pixels (C); 8) gamma-MAP spatial filtering 3x3 pixels (S); 9) geo-coding and sigma nought calibration (S); 10) masking of the layover and shadow by considering the local incidence angle (LIA) for each pixel (C). It is worth noting that we use the multi-temporal filter proposed by (Quegan and Yu, 2001). This filter, which is suited for long time-series, allows a suppression of the speckle noise by preserving at the same time the geometrical detail. The final spatial resolution of the geo-coded S-1 images is 20 by 20 meters.

## 4 Data analysis and proposed approach to the melting phases identification from S-1

In this section, the time-series of SWE, LWC and $\sigma^0$ for the identification of the melting phases are compared. From this analysis and the background information described in section 2, we present the general temporal evolution of the backscattering during the melting process. Finally, on the basis of this analysis we propose a set of simple rules for the derivation of the onsets of each snow melting phase.

### 4.1 Data analysis

Figure 4 shows the time series of the backscattering coefficient against the measured and/or modeled SWE and LWC for the five test sites during the hydrological years 2016/2017 (left column) and 2017/2018 (right column). Yellow, red and green areas highlight the moistening, ripening and run-off phases respectively. These phases have been identified from the SWE and LWC data according to section 2.1. In the following, for each of the five test sites i.e., Zugspitze, Alpe Tumolo, Clozner Loch, Malga Fadner and Weissfluhjoch, we will present the detailed comparison of LWC, SWE and the S-1 $\sigma^0$ time series during the melting process. This will allow the derivation of important information about the possibility to identify the three melting phases in general. In the next section, the outcome of this comparison will be exploited to describe the characteristic behavior of the multi-temporal SAR signal during the melting process.

#### 4.1.1 Zugspitze

For this station, SWE was both measured and simulated and LWC was simulated with SNOWPACK. The temporal evolution of SWE measured by the snow scale and the one simulated with SNOWPACK shows a good agreement. For this station, the tracks T168 (descending, morning) and T117 (ascending, afternoon) are available. The local incidence angle for the two tracks differs of about 1 degree. For the hydrological year 2016/2017 the backscattering remains almost constant during the accumulation phase till the beginning of the moistening phase (Figure 4a). Here, as described in section 2.2, the increase of the LWC is accompanied by a decrease of the backscattering from -8.5 dB and -12.7 dB to -14.3 dB and -20.0 dB for respectively VV and VH of the afternoon track T117 between the 19th and the 25th of March 2017 and from -5.8 dB and -12.7 dB to -12.5 dB and -18.1 dB for respectively VV and VH of the morning track T168 between the 27th of March and the 4th of April. The difference in the dropping of the signal acquired by the morning and afternoon track is due to the diurnal melting and refreezing cycles. After this phase, the ripening phase began with oscillations of the backscattering coefficient which on average presented low values. As described in section 2.2 the oscillations are due to the snowpack metamorphism, snow stratification and the meteorological conditions. Since the ripening phase is characterized by an increase of the LWC, the time series of the backscattering presents a decreasing trend. Interestingly, the minimum of $\sigma^0$ is reached in correspondence to the finishing of the ripening phase and the beginning of the run-off phase i.e., 20th of May 2017. The run-off is instead characterized by a monotonic increase of the backscattering till all snow is melted. This characteristic behavior can be interpreted as follow: when the considered snowpack reaches its saturation condition in terms of the LWC, snow density and internal structure, the backscattering recorded in C-band reaches its minimum value. These snowpack conditions seems to represent the isothermal condition before the release of melt water i.e., the end of the ripening phase. After the saturation point is reached, the monotonic increase of $\sigma^0$ could be explained by a dominance of the superficial scattering that becomes more and more prominent due to a monotonic increase of the LWC per volume (see section 2.2). This behavior continues until the snow disappears. This period corresponds to the runoff formation phase, when SWE starts decreasing. In section 4.2 we will discuss a possible explanation of this apparently surprising behavior. Regarding the winter 2017/2018 similar observations were made, but here the snow ripening phase was limited to a very short period and the run-off started very early in mid-April due to strong insolation and high mean daily temperatures up to 5°C the days before. Interestingly, during the run-off phase, $\sigma^0$ started increasing as expected, then it decreased in correspondence of a snow fall (probably wet) followed by a relatively colder period which lasted some days at the end of May 2018 and finally it increased again till the end of the snow season (Figure 4b).

It is worth noting that the two polarizations acquired by S-1 provided coherent information. However, few cases in which there is a depolarization of the signal can be spotted during the ripening phase. Here the repeated cycles of melting and refreezing can generate ice layers (Kattelmann and Dozier, 1999), which affect the polarization in different ways.

### 4.1.2 Alpe del Tumulo

For this station, the information about the LWC and SWE were derived through SNOWPACK. The calibration of the model was performed in order to achieve a high agreement in terms of snow height and snow temperature (see Table 3). For this station, the tracks T168 (descending, morning), T117 (ascending, afternoon) and T095 (descending, morning) are available. The LIAs for the three tracks are 40, 35 and 47 degrees, respectively.

A very short moistening phase can be identified in both years from the modeled LWC and SWE time series (Figure 4c, 4d). These phases are well identified in the $\sigma^0$ time series by a drop of the morning and afternoon signal. The situation of the run-off phase 2016/2017 looks similar to Zugspitze for the season 2017/2018: from the LWC and SWE time series two modes are visible suggesting that the run-off was stopped by a cold period (with a new snowfall). This situation is reflected in the time series of the S-1 backscattering by the two characteristic “U-shaped” behaviors indicating that a first run-off started after the first minimum of $\sigma^0$ and continued for some days in correspondence of the monotonic increase of $\sigma^0$, but then the process was stopped by a new wet snowfall that forced the backscattering to a new minimum. Finally, the run-off phase restarted, and the SAR signal increased again. However, the runoff phases identified from the SAR local minima seem to be anticipated by about two weeks with respect to the modeling results. Regarding the season 2017/2018, the run-off phase showed a more linear behavior which is represented by the characteristic shape of $\sigma^0$ time series as the one identified in the Zugspitze test site. It is finally worth noting that, the three tracks (T095 and T168, descending, and T117, ascending) acquired with different LIA show very similar trends.

### 4.1.3 Clozner Loch

For this station, the information about the LWC and SWE were simulated with the SNOWPACK model. The calibration of the model was performed in order to achieve a high agreement in terms of snow height and snow temperature (see Table 3). The tracks T168 (descending, morning), T117 (ascending, afternoon) and T095 (descending, morning) are available for this station. The LIAs for the three tracks are 43, 36 and 39 degrees, respectively.

The season 2016/2017 is characterized by two melting phases (Figure 4e). In fact, the snow was completely melted in the first half of April with a new fresh snowfall at the end of the month. For this reason, we highlighted two different times the snowpack alteration sequence moistening – ripening – run-off. Interestingly, the time series of the backscattering seems to properly follow the two melting processes with two characteristic "U-shaped" behaviors. The melting process for the season 2017/2018 was more linear (Figure 4f) and the $\sigma^0$ time series of the three tracks provides coherent information with the one extracted by analyzing the time series of LWC and SWE.

### 4.1.4 Malga Fadner

For this station, the information about the LWC and SWE were derived through the SNOWPACK model. The calibration of the model was performed in order to achieve a high agreement in terms of snow height and snow temperature (see Table 3). Four tracks are available for this station: T168 (descending, morning), T117 (ascending, afternoon), T044 (ascending, afternoon) and T095 (descending, morning). The LIAs for the three tracks are 46, 48, 38 and 34 degrees, respectively.

The trend of the melting process over the two seasons looks similar to Alpe del Tumulo. The season 2016/2017 is characterized by a consistent snowfall, which happened after an initial run-off phase of the snowpack. This together with a cold period, stopped the process, which was resumed in May (Figure 4g). The time series of the four tracks recorded by S-1 backscattering showed two characteristic "U-shaped" behavior indicating that a first run-off started after the first minimum of $\sigma^0$ and continued for some days in correspondence of the monotonic increase of $\sigma^0$, but then the process was stopped by a new wet snowfall that forced the backscattering again to the minimum. Nonetheless, the timings are different from the one identified with the modeled data of LWC and SWE. The strong depolarization may indicate a complex structure of the snowpack with different ice layers. The melting process for the season 2017/2018 was more linear and the $\sigma^0$ time series of the four tracks provides coherent information with the one extracted by analyzing the time series of LWC and SWE (Figure 4e).

### 4.1.5 Weissfluhjoch

For this station, the information about the LWC and SWE were simulated with SNOWPACK, additionally SWE GPS-derived measurements were available. The calibration of the model was performed in order to achieve a high agreement in terms of snow height and SWE (see Table 3). The tracks T168 (descending, morning), T117 (ascending, afternoon), T015 (ascending, afternoon) and T066 (descending, morning) are available for this station. The LIAs for the three tracks are 41, 33, 43 and 31 degrees, respectively.

https://doi.org/10.5194/tc-2019-175
Preprint. Discussion started: 4 September 2019

The season 2016/2017 is characterized by an initial moistening phase, followed by a ripening phase that was delayed by a cold period, when the LWC decreases almost to 0 (Figure 4i). In the middle of May a runoff phase started. The backscattering followed the different phases as expected. The season 2017/2018 is more regular, with a monotonic increasing of LWC indicating a short moistening followed by a regular ripening and the runoff. In this case the measured SWE anticipated the runoff onset of about one week w.r.t. the modeled SWE, which seems more in accordance with the S-1 data. The backscattering shows a similar behavior of other previously discussed cases with the characteristic “U-shaped” signal except for the T066 that present several oscillations in the VH polarization.

### 4.2 Theoretical Temporal Evolution of the Backscattering

From the comparison carried out in the previous section and by taking into account the main backscattering mechanisms described in section 2.2, it is possible to derive and explain the temporal behavior of $\sigma^0$ generated by a C-band SAR over a sufficiently deep snowpack located in an open space that present a linear transition between the three melting phases. By analyzing the backscattering time series of the same pixel, the contribution of the LIA is always the same, making the values of the time series comparable. Figure 5 shows the theoretical temporal evolution of $\sigma^0$ for a complete hydrological year. Before the snow cover the terrain, $\sigma^0$ is influenced by the fluctuation of the soil moisture (Ulaby et al., 1996). Then, generally the first snow fall is wet or it covers relatively warm terrain resulting in a wet snowpack. This generates low backscattering values in the SAR response. This situation, which in alpine environments usually lasts for short periods, ends either with a significant decrease of the temperature that brings the snowpack to a dry condition or with a complete melting of the snowpack. It is also possible that the soil freezes before the first snowfalls. In this case the coefficient of backscattering decreases and stabilizes around a given value, not being affected by the soil moisture anymore.

As soon as the snowpack starts incorporating liquid water, the melting period starts. It can be divided into three important phases as described in section 2.1 i.e., the moistening, the ripening and the runoff phases. The first phase is related to the initial moistening of the snowpack. As discussed previously, the liquid water is introduced in the snow by rain and/or melt due to temperature and the incoming flux of shortwave radiation. At the beginning of the process the value of LWC is low and therefore the SAR backscattering experiences a relevant decrease in its value since the volumetric scattering dominates the total backscattering. The drop of the signal is recognizable by imposing a given threshold $T$. During the moistening, the wetting front may be visible only during the afternoon and not in the morning since the snowpack is still subjected to the diurnal cycles of melting and refreezing. As soon as the wetting front has penetrated the superficial insulating layer of the snowpack, the wet snow becomes visible also in the SAR early morning acquisitions. Please note that the systematic offset between the morning and afternoon signals represents the generally different local incidence angle of the ascending and descending acquisitions in mountainous region. At this point the phase of snowpack ripening starts. In this phase, the wetting front keeps penetrating the snowpack conducting it to an isothermal condition. During the ripening phase, which is influenced by the weather and the snowpack conditions, $\sigma^0$ varies according to the snow conditions but with an overall decreasing trend due to the increase of LWC. During the snow ripening, depolarization of the VV and VH signals recorded by S-1 may indicate the presence of ice layers in the snowpack.

We observed that the minimum of $\sigma^0$ is reached in correspondence of the finishing of the ripening phase and the beginning of the run-off phase for all the ten time series observed (see section 5). The run-off is instead characterized by a monotonic increase of the backscattering till all the snow is melted. To our knowledge, this characteristic behavior has been never observed in the literature before. Our interpretation is as follow: when the considered snowpack reaches its saturation condition in terms of LWC and snow structure, the backscattering recorded in C-band reaches its minimum value. This snowpack condition seems to correspond with the isothermal condition i.e., the end of the ripening phase. After the saturation point is reached, the monotonic increase of $\sigma^0$ could be explained by one or the combination of the following factors: i) an increase of the superficial roughness; ii) a change in the snow structure i.e., increase of the density and increase of grain size and; iii) at the end of the melting, the presence of patchy snow creates a situation of mixed contribution inside the resolution cell of the SAR and therefore a further increase of the total backscattering is recorded.

On the basis of the previously discussed observations, we propose here a simple set or rules to identify the snow melting phases on the basis of the multi-temporal SAR signal. The start of the melting process can be identified by a decrease of the multi-temporal SAR signal recorded in the afternoon of 2 dB or more w.r.t. the general winter trend. This threshold has been also proposed by (Nagler et al., 2016). As soon as also the backscattering time series recorded in the morning experience a decrease of more than 2 dB, we assume that the ripening phase begins. This phase, characterized by several oscillations, ends when both the morning and afternoon $\sigma^0$ reach their local minimum. We propose the mean date among the local minima as the start of the run-off phase, which is characterized by a monotonic increase of the coefficient of backscattering.

In the next section we applied these simple set of rules in order to identify the melting phases for each of the five considered test sites. Moreover, the same rules are used to identify the run-off onset for each SAR pixel in the topographically well-defined catchment of the Zugspitzplatt obtaining a spatially distributed map of the run-off timing.

## 5 Validation of the proposed approach and a spatially distributed application

In this section, we present the results obtained for the snow melting phases identification from the time series of backscattering recorded from S-1 over the five selected alpine test sites. The results are compared with the derivation of the melting phases considering the observed and modeled measurements of LWC and SWE. Finally, we present the result of the run-off onset identification in the two dimensional space of the original 20 meters SAR images for the Zugspitze catchment.

### 5.1 Identification of snow phases from Sentinel-1 in the five alpine test sites

Table 5 reports the comparison of the onset dates for the melting phases for each of the considered test sites. The phases were identified from the backscattering time series according to the rules expressed in the previous section. If more than two acquisitions i.e., ascending and descending are available for one test site, the first date representing the onset for the moistening and ripening phase among all available tracks is selected. The runoff onset is identified as the mean date among the local minima. These rules can be automatically applied without any human supervision.

https://doi.org/10.5194/tc-2019-175
Preprint. Discussion started: 4 September 2019

On average, the moistening phase was identified with a r.m.s. error of 6.5 days. For the ripening phase the SAR time series allowed the identification with 4.5 days of r.m.s. error. Finally, the run-off was identified with a r.m.s. of 8 days (4 days r.m.s. error without considering Alpe del Tumolo for the years 2016/2017 and Weissfluhjoch for the years 2017/2018 where the runoff process were articulated). Considering the repetition frequency provided by S-1 and the possible uncertainty of the SNOWPACK modeling (Wever et al., 2015), the produced results demonstrate the effectiveness of using the SAR for characterizing the snow melt process.

In some cases, the proposed rules could not be applied and the onset could not be identified from the S-1 data. This is mainly due to the short melting or ripening periods that occurred during some years in the selected test sites. In these cases, the 6 days repetitions provided by S-1 is not adequate to sample this situation and it happens that the moistening phase is captured by the morning acquisition before than the afternoon acquisition (i.e., Zugspitze season 2016/2017 and 2017/2018, Clozner Loch season 2016/2017 second moistening phase and 2017/2018) or the first signal drop is reached at the same time of the local minima (i.e., Clozner Loch season 2017/2018). One can also notice that, for the first runoff identified in the season 2016/2017 for Malga Fadner, the proposed rules failed since for T168 no local minimum was clearly identified (Figure 4g).

### 5.2 Extension to a 2D analysis of the run-off onset: the Zugspitzplatt catchment

In this section we evaluate how the identification of the run-off onset is performed at a catchment scale. In particular, we considered the multi-temporal behavior of each pixel acquired by S-1 over the Zugspitzplatt during the hydrological year 2017/2018. The plateau (1500-2700 $\mathrm{m}$ a.s.l.) on the southern slope of Mt. Zugspitze summit (2962 $\mathrm{m}$ a.s.l.) is well suited for this application scenario, since it is proven that all surface and ground water is drained to the Reintal valley in the east by the Partnach River (Rappl et al., 2010). With regard to a potential transport of contaminants that are stored in the snowpack and released with the first snowmelt (Hürkamp, Tafelmeier and Tschiersch, 2017), the knowledge of the run-off onset can provide important information for the scope of action concerning the management of countermeasures or planning actions to mitigate potential soil and water contamination.

As illustrated in the previous section, the run-off onset was identified by locating the minimum of the backscattering time series. In order to increase the robustness of the detection, we considered the mean of backscattering of close pixel presenting the same characteristics in terms of altitude, exposition and slopes. In detail, belts of 100 $\mathrm{m}$ were considered for the altitude. Slope was divided in three classes between 0-20, 20-40 and 40-60 degrees. Four aspect classes were considered, i.e. North, East, South and West. Finally, a local incidence angle ranging from 25 to 65 degrees was divided in 8 classes with 5 degrees span, avoiding layover and shadow effects. All the homogeneous classes generated by the different combinations were aggregated. The forested areas were masked using the Copernicus tree cover density map (https://land.copernicus.eu/pan-european/high-resolution-layers/forests/tree-cover-density/status-maps/2015). Moreover, since in this illustrative example we are interested in the main runoff contribution, the proposed algorithm is looking for local minima of the backscattering time series only after January 2018. This to exclude isolated wet snowfalls or complete early melting events typical of the beginning of the seasons.

Figure 6 shows the run-off onset identified by the proposed method. As one can notice, the regions at lower altitude started the run-off phase before the areas at higher altitude. The same consideration can be done for the pixels north exposed versus the south exposed ones. Interestingly, the last areas that start the run-off phase in the catchment are the glacierized areas (Northern and Southern Schneeferner glacier) and north faced slope areas. A selection of the backscattering time series is reported at the bottom of the Figure 6 for six points selected at different altitudes. As one can notice the characteristic behavior described in section 4.2 is always visible in the real data.

## 6 Conclusions

In this paper, we analyzed the correlation between the multi-temporal SAR backscattering and the snow melt dynamics. We compared Sentinel-1 backscattering with LWC and SWE measurements derived from in situ observations and process-based snow modeling simulations for five alpine test sites in Italy, Germany and Switzerland considering two hydrological years. We found that the multi-temporal SAR measurements allow the identification of the three melting phases that characterize the melting process i.e., moistening, ripening and runoff with a good agreement considering the revisit time of Sentinel-1. In detail, we found that in the considered sites the SAR backscattering decreases as soon as the snow starts containing water, and that the backscattering increases as soon as SWE starts decreasing, which corresponds to the release of meltwater from the snowpack. We discuss the possible reasons of this increase, which are not directly correlated to the SWE decrease, but most probably to the different snow conditions, which change the backscattering mechanisms. From this study we define a set of simple rules that can be applied to the multi-temporal SAR backscattering in order to identify the melting phases. We showed that by applying these rules, the identification of the melting phases was possible for the five considered test sites with an rmse of 6 days for the moistening phase, 4 days for the ripening and 7 days for the runoff phase. Moreover, the same rules were applied for the identification of the run-off onset for the entire Zugspitzplatt catchment with reasonable results even if further hydrological analyses have to be performed. The presented investigation could have relevant application for monitoring and predicting the snowmelt progress over large regions. A better understanding of the spatial and temporal evolution of melting dynamics in mountain regions and the knowledge on the onset of melt water runoff can help to predict floods and define the scope of action to mitigate potential contaminant distributions in soils and surface water.

As future developments we plan to develop and test an automatic method to identify the three melting phases of a snowpack using larger validation dataset (e.g., Snowtel) and allow to proper discuss the spatial and temporal evolution of snow water content and run-off in mountainous region. Moreover, we investigate the reasons of the increase of the backscattering in correspondence of the decrease of SWE through in situ experiments that take into account the hypothesis expressed in this paper.

*Data availability.* Relevant data can be made available upon request to the authors. All the Sentinel-1 data are freely available at https://scihub.copernicus.eu/ upon registration.

*Author contributions.* CM, MC and GB designed the research; VP carried out all the experiments and run the SNOWPACK model; all the authors contributed to the analysis and interpretation of the results; CM wrote the paper based on inputs and feedbacks from all co-authors.

*Competing interests.* Authors declare no competing interests.

*Acknowledgements.* We thank the Bavarian Avalanche Warning Service (Lawinenwarnzentrale Bayern) and the Environmental Research Station Schneefernerhaus (UFS) for providing the measurement data for the German test site Zugspitze, the Hydrografic office of the Autonomous province of Bolzano for providing the data for the Italian test sites of Alpe Tumulo, Clozner Loch and Fadner Alm and the WSL insitute for snow and avalanche research SLF for providing the data for the Switzerland test site Weissfluhjoch. The work of the MC and GB were financed through the CRYOMON-SciPro project, founded by the Euregio Science Fund 1st call, project number IPN 10. Parts of the measurements and snow sensor installations at the Zugspitze station were funded by the Bavarian Ministry of the Environment and Consumer Protection (BayStMUV) in the framework of the Virtual Alpine Observatory (VAO) project.

## References

Avanzi, F., De Michele, C., Morin, S., Carmagnola, C. M., Ghezzi, A., and Lejeune, Y.: Model complexity and data requirements in snow hydrology: seeking a balance in practical applications, Hydrological Processes, 30, 2106–2118, https://doi.org/10.1002/hyp.10782, http://doi.wiley.com/10.1002/hyp.10782, 2016.

Baghdadi, N., Gauthier, Y., Bernier, M., and Fortin, J.-P.: Potential and limitations of RADARSAT SAR data for wet snow monitoring, IEEE Transactions on Geoscience and Remote Sensing, 38, 316–320, https://doi.org/10.1109/36.823925, http://ieeexplore.ieee.org/document/823925/, 2000.

Bartelt, P. and Lehning, M.: A physical SNOWPACK model for the Swiss avalanche warning: Part I: numerical model, Cold Regions Science and Technology, 35, 123–145, https://doi.org/10.1016/S0165-232X(02)00074-5, https://www.sciencedirect.com/science/article/pii/S0165232X02000745, 2002.

Bavay, M. and Egger, T.: MeteoIO 2.4.2: a preprocessing library for meteorological data, Geoscientific Model Development, 7, 3135–3151, https://doi.org/10.5194/gmd-7-3135-2014, http://www.geosci-model-dev.net/7/3135/2014/, 2014.

Bellaire, S., van Herwijnen, A., Mitterer, C., and Schweizer, J.: On forecasting wet-snow avalanche activity using simulated snow cover data, Cold Regions Science and Technology, 144, 28–38, https://doi.org/10.1016/J.COLDREGIONS.2017.09.013, https://www.sciencedirect.com/science/article/pii/S0165232X17301891, 2017.

Beniston, M., Farinotti, D., Stoffel, M., Andreassen, L. M., Coppola, E., Eckert, N., Fantini, A., Giacona, F., Hauck, C., Huss, M., Huwald, H., Lehning, M., López-Moreno, J.-I., Magnusson, J., Marty, C., Morán-Tejéda, E., Morin, S., Naaim, M., Provenzale, A., Rabatel, A., Six, D., Stötter, J., Strasser, U., Terzago, S., and Vincent, C.: The European mountain cryosphere: a review of its current state, trends, and future challenges, The Cryosphere, 12, 759–794, https://doi.org/10.5194/tc-12-759-2018, https://www.the-cryosphere.net/12/759/2018/, 2018.

Brun, E., David, P., Sudul, M., and Brunot, G.: A numerical model to simulate snow-cover stratigraphy for operational avalanche forecasting, Journal of Glaciology, 38, 13–22, https://doi.org/10.3189/S0022143000009552, https://www.cambridge.org/core/product/identifier/S0022143000009552/type/journal{_}article, 1992.

DeWalle, D. R. and Rango, A.: Principles of Snow Hydrology, Cambridge University Press, Cambridge, https://doi.org/10.1017/CBO9780511535673, https://www.cambridge.org/core/product/identifier/9780511535673/type/book, 2008.

Dilley, A. C. and O'brien, D. M.: Estimating downward clear sky long-wave irradiance at the surface from screen temperature and precipitable water, Quarterly Journal of the Royal Meteorological Society, 124, 1391–1401, https://doi.org/10.1002/qj.49712454903, https://rmets.onlinelibrary.wiley.com/doi/abs/10.1002/qj.49712454903, 1998.

Dingman, S.: Physical hydrology, Waveland press, 2015.

Dong, C.: Remote sensing, hydrological modeling and in situ observations in snow cover research: A review, Journal of Hydrology, 561, 573–583, https://doi.org/10.1016/J.JHYDROL.2018.04.027, https://www.sciencedirect.com/science/article/pii/S0022169418302804{#}!, 2018.

Endrizzi, S., Gruber, S., Dall&apos;Amico, M., and Rigon, R.: GEOtop 2.0: simulating the combined energy and water balance at and below the land surface accounting for soil freezing, snow cover and terrain effects, Geoscientific Model Development, 7, 2831–2857, https://doi.org/10.5194/gmd-7-2831-2014, https://www.geosci-model-dev.net/7/2831/2014/, 2014.

Engel, M., Notarnicola, C., Endrizzi, S., and Bertoldi, G.: Snow model sensitivity analysis to understand spatial and temporal snow dynamics in a high-elevation catchment, Hydrological Processes, 31, 4151–4168, https://doi.org/10.1002/hyp.11314, http://doi.wiley.com/10.1002/hyp.11314, 2017.

Essery, R., Morin, S., Lejeune, Y., and B Ménard, C.: A comparison of 1701 snow models using observations from an alpine site, Advances in Water Resources, 55, 131–148, https://doi.org/10.1016/J.ADVWATRES.2012.07.013, https://www.sciencedirect.com/science/article/pii/S0309170812002011, 2013.

Fassnacht, S., Williams, M., and Corrao, M.: Changes in the surface roughness of snow from millimetre to metre scales, Ecological Complexity, 6, 221–229, https://doi.org/10.1016/J.ECOCOM.2009.05.003, https://www.sciencedirect.com/science/article/pii/S1476945X09000567, 2009.

Fromm, R., Baumgärtner, S., Leitinger, G., Tasser, E., and Höller, P.: Determining the drivers for snow gliding, Natural Hazards and Earth System Sciences, 18, 1891–1903, https://doi.org/10.5194/nhess-18-1891-2018, https://www.nat-hazards-earth-syst-sci.net/18/1891/2018/, 2018.

Günther, D., Marke, T., Essery, R., and Strasser, U.: Uncertainties in Snowpack Simulations—Assessing the Impact of Model Structure, Parameter Choice, and Forcing Data Error on Point-Scale Energy Balance Snow Model Performance, Water Resources Research, 55, 2779–2800, https://doi.org/10.1029/2018WR023403, https://onlinelibrary.wiley.com/doi/abs/10.1029/2018WR023403, 2019.

Hirashima, H., Yamaguchi, S., Sato, A., and Lehning, M.: Numerical modeling of liquid water movement through layered snow based on new measurements of the water retention curve, Cold Regions Science and Technology, 64, 94–103, https://doi.org/10.1016/J.COLDREGIONS.2010.09.003, https://www.sciencedirect.com/science/article/pii/S0165232X10001722, 2010.

Hürkamp, K., Tafelmeier, S., and Tschiersch, J.: Influence of melt-freeze-cycles on the radionuclide transport in homogeneous laboratory snowpack, Hydrological Processes, 31, 1360–1370, https://doi.org/10.1002/hyp.11110, http://doi.wiley.com/10.1002/hyp.11110, 2017.

Hürkamp, K., Zentner, N., Reckerth, A., Weishaupt, S., Wetzel, K.-F., Tschiersch, J., and Stumpp, C.: Spatial and Temporal Variability of Snow Isotopic Composition on Mt. Zugspitze, Bavarian Alps, Germany, Journal of Hydrology and Hydromechanics, 67, 49–58, https://doi.org/10.2478/johh-2018-0019, http://content.sciendo.com/view/journals/johh/67/1/article-p49.xml, 2019.

Kinar, N. J. and Pomeroy, J. W.: Measurement of the physical properties of the snowpack, Reviews of Geophysics, 53, 481–544, https://doi.org/10.1002/2015RG000481, http://doi.wiley.com/10.1002/2015RG000481, 2015.

Koch, F., Prasch, M., Schmid, L., Schweizer, J., and Mauser, W.: Measuring Snow Liquid Water Content with Low-Cost GPS Receivers, Sensors, 14, 20 975–20 999, https://doi.org/10.3390/s141120975, http://www.mdpi.com/1424-8220/14/11/20975, 2014.

Koch, F., Henkel, P., Appel, F., Schmid, L., Bach, H., Lamm, M., Prasch, M., Schweizer, J., and Mauser, W.: Retrieval of Snow Water Equivalent, Liquid Water Content, and Snow Height of Dry and Wet Snow by Combining GPS Signal Attenuation and Time Delay, Water Resources Research, 55, 4465–4487, https://doi.org/10.1029/2018WR024431, https://agupubs.onlinelibrary.wiley.com/doi/abs/10.1029/2018WR024431, 2019.

Koskinen, J., Pulliainen, J., Luojus, K., and Takala, M.: Monitoring of Snow-Cover Properties During the Spring Melting Period in Forested Areas, IEEE Transactions on Geoscience and Remote Sensing, 48, 50–58, https://doi.org/10.1109/TGRS.2009.2024755, http://ieeexplore.ieee.org/document/5238521/, 2010.

Lehning, M., Völksch, I., Gustafsson, D., Nguyen, T. A., Stähli, M., and Zappa, M.: ALPINE3D: a detailed model of mountain surface processes and its application to snow hydrology, Hydrological Processes, 20, 2111–2128, https://doi.org/10.1002/hyp.6204, http://doi.wiley.com/10.1002/hyp.6204, 2006.

Longepe, N., Allain, S., Ferro-Famil, L., Pottier, E., and Durand, Y.: Snowpack Characterization in Mountainous Regions Using C-Band SAR Data and a Meteorological Model, IEEE Transactions on Geoscience and Remote Sensing, 47, 406–418, https://doi.org/10.1109/TGRS.2008.2006048, http://ieeexplore.ieee.org/document/4768720/, 2009.

Magagi, R. and Bernier, M.: Optimal conditions for wet snow detection using RADARSAT SAR data, Remote Sensing of Environment, 84, 221–233, https://doi.org/10.1016/S0034-4257(02)00104-9, https://www.sciencedirect.com/science/article/pii/S0034425702001049, 2003.

Mair, E., Leitinger, G., Della Chiesa, S., Niedrist, G., Tappeiner, U., and Bertoldi, G.: A simple method to combine snow height and meteorological observations to estimate winter precipitation at sub-daily resolution, Hydrological Sciences Journal, 61, 2050–2060, https://doi.org/10.1080/02626667.2015.1081203, https://www.tandfonline.com/doi/full/10.1080/02626667.2015.1081203, 2016.

Mott, R., Egli, L., Grünewald, T., Dawes, N., Manes, C., Bavay, M., and Lehning, M.: Micrometeorological processes driving snow ablation in an Alpine catchment, The Cryosphere, 5, 1083–1098, https://doi.org/10.5194/tc-5-1083-2011, https://www.the-cryosphere.net/5/1083/2011/, 2011.

Nagler, T. and Rott, H.: Retrieval of wet snow by means of multitemporal SAR data, IEEE Transactions on Geoscience and Remote Sensing, 38, 754–765, https://doi.org/10.1109/36.842004, 2000.

Nagler, T., Rott, H., Ripper, E., Bippus, G., and Hetzenecker, M.: Advancements for Snowmelt Monitoring by Means of Sentinel-1 SAR, Remote Sensing, 8, 348, https://doi.org/10.3390/rs8040348, http://www.mdpi.com/2072-4292/8/4/348, 2016.

Pomeroy, J. and Brun, E.: Physical properties of snow, in: Snow Ecology: An Interdisciplinary Examination of Snow-Covered Ecosystems, edited by H. G. Jones et al., pp. 45–126, Cambridge Univ. Press, Cambridge, U. K., 2001.

Quegan, S. and Yu, J. J.: Filtering of multichannel SAR images, IEEE Transactions on Geoscience and Remote Sensing, 39, 2373–2379, https://doi.org/10.1109/36.964973, 2001.

Raleigh, M. S., Lundquist, J. D., and Clark, M. P.: Exploring the impact of forcing error characteristics on physically based snow simulations within a global sensitivity analysis framework, Hydrology and Earth System Sciences, 19, 3153–3179, https://doi.org/10.5194/hess-19-3153-2015, https://www.hydrol-earth-syst-sci.net/19/3153/2015/, 2015.

Rott, H. and Mätzler, C.: Possibilities and limits of synthetic aperture radar for snow and glacier surveying, Annals of Glaciology, http://www.ingentaconnect.com/contentone/igsoc/agl/1987/00000009/00000001/art00032, 1987.

Schmid, L., Heilig, A., Mitterer, C., Schweizer, J., Maurer, H., Okorn, R., and Eisen, O.: Continuous snowpack monitoring using upward-looking ground-penetrating radar technology, Journal of Glaciology, 60, 509–525, https://doi.org/10.3189/2014JoG13J084, https://www.cambridge.org/core/product/identifier/S0022143000205984/type/journal{_}article, 2014.

Sevruk, B., Ondrás, M., and Chvíla, B.: The WMO precipitation measurement intercomparisons, Atmospheric Research, 92, 376 – 380, https://doi.org/https://doi.org/10.1016/j.atmosres.2009.01.016, http://www.sciencedirect.com/science/article/pii/S0169809509000337, 7th International Workshop on Precipitation in Urban Areas, 2009.

Shi, J. and Dozier, J.: Measurements of snow-and glacier-covered areas with single-polarization SAR, Annals of glaciology, http://www.ingentaconnect.com/content/igsoc/agl/1993/00000017/00000001/art00010, 1993.

Shi, J. and Dozier, J.: Inferring snow wetness using C-band data from SIR-C's polarimetric synthetic aperture radar, IEEE Transactions on Geoscience and Remote Sensing, 33, 905–914, https://doi.org/10.1109/36.406676, http://ieeexplore.ieee.org/document/406676/, 1995.

Stähli, M., Stacheder, M., Gustafsson, D., Schlaeger, S., Schneebeli, M., and Brandelik, A.: A new in situ sensor for large-scale snow-cover monitoring, Annals of Glaciology, 38, 273–278, https://doi.org/10.3189/172756404781814933, https://www.cambridge.org/core/product/identifier/S0260305500256127/type/journal{_}article, 2004.

Strasser, U., Warscher, M., and Liston, G. E.: Modeling Snow–Canopy Processes on an Idealized Mountain, Journal of Hydrometeorology, 12, 663–677, https://doi.org/10.1175/2011JHM1344.1, http://journals.ametsoc.org/doi/abs/10.1175/2011JHM1344.1, 2011.

Techel, F. and Pielmeier, C.: Point observations of liquid water content in wet snow - investigating methodical, spatial and temporal aspects, The Cryosphere, 5, 405–418, https://doi.org/10.5194/tc-5-405-2011, http://www.the-cryosphere.net/5/405/2011/, 2011.

Ulaby, F., Moore, R., and Fung, A.: Microwave remote sensing active and passive, http://bibliotecadigital.ciren.cl/handle/123456789/19995, 2015.

Ulaby, F. T., Dubois, P. C., and van Zyl, J.: Radar mapping of surface soil moisture, Journal of Hydrology, 184, 57–84, https://doi.org/10.1016/0022-1694(95)02968-0, https://www.sciencedirect.com/science/article/pii/0022169495029680, 1996.

Unsworth, M. H. and Monteith, J. L.: Long-wave radiation at the ground I. Angular distribution of incoming radiation, Quarterly Journal of the Royal Meteorological Society, 101, 13–24, https://doi.org/10.1002/qj.49710142703, https://rmets.onlinelibrary.wiley.com/doi/abs/10.1002/qj.49710142703, 1975.

Viviroli, D. and Weingartner, R.: The hydrological significance of mountains: from regional to global scale, Hydrology and Earth System Sciences, 8, 1017–1030, https://doi.org/10.5194/hess-8-1017-2004, http://www.hydrol-earth-syst-sci.net/8/1017/2004/, 2004.

Wehren, B., Weingartner, R., Schädler, B., and Viviroli, D.: General Characteristics of Alpine Waters, pp. 17–58, Springer, Berlin, Heidelberg, https://doi.org/10.1007/978-3-540-88275-6_2, http://link.springer.com/10.1007/978-3-540-88275-6{_}2, 2010.

Wever, N., Fierz, C., Mitterer, C., Hirashima, H., and Lehning, M.: Solving Richards Equation for snow improves snowpack meltwater runoff estimations in detailed multi-layer snowpack model, The Cryosphere, 8, 257–274, https://doi.org/10.5194/tc-8-257-2014, https://www.the-cryosphere.net/8/257/2014/, 2014.

Wever, N., Schmid, L., Heilig, A., Eisen, O., Fierz, C., and Lehning, M.: Verification of the multi-layer SNOWPACK model with different water transport schemes, The Cryosphere, 9, 2271–2293, https://doi.org/10.5194/tc-9-2271-2015, https://www.the-cryosphere.net/9/2271/2015/, 2015.

WSL Institute for Snow and Avalanche Research SLF: WFJ_MOD: Meteorological and snowpack measurements from Weissfluhjoch, Davos, Switzerland", https://doi.org/http://dx.doi.org/10.16904/1, https://www.envidat.ch/dataset/10-16904-1, 2015.

https://doi.org/10.5194/tc-2019-175
Preprint. Discussion started: 4 September 2019

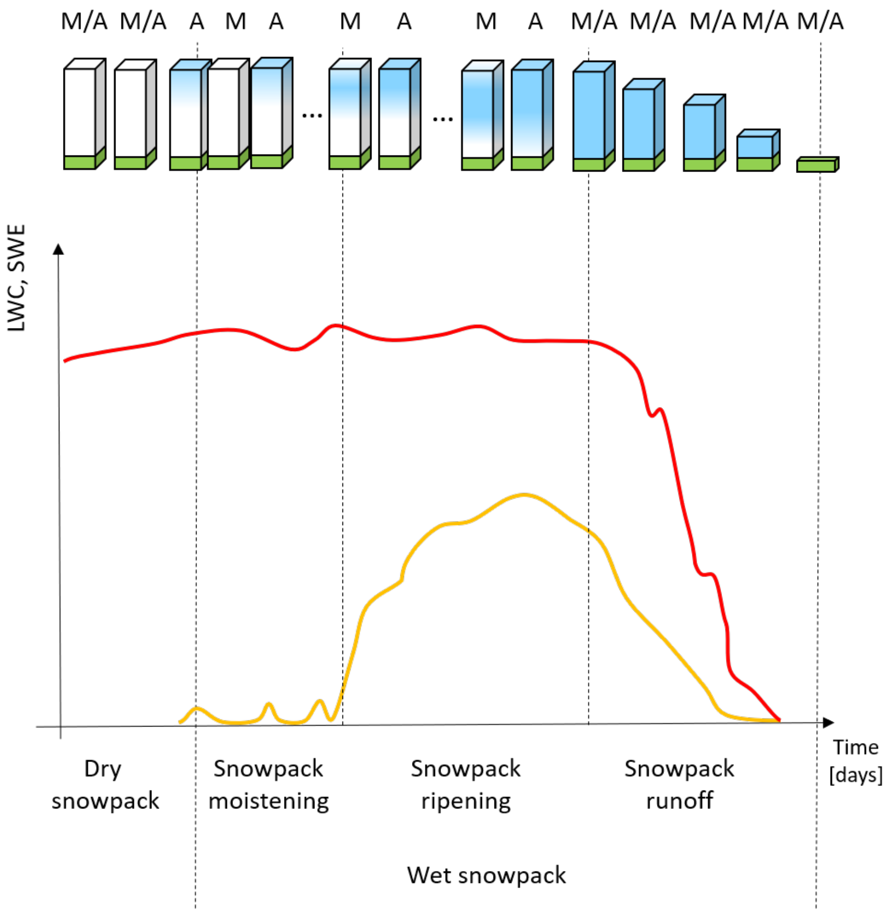

**Figure 1.** Example of transitions in snow status during the melting season obtained by sampling the snow in the morning (M), when the S-1 descending observations are taken, and in the evening (A) when the S-1 ascending data are taken. The upper part of the figure illustrates the simplified temporal transportation of the free liquid water (blue area) in the dry snowpack (white area). The lower part of the figure illustrates the respective temporal evolution of LWC (yellow line) and SWE (red line). In detail, by starting from a dry situation, the liquid water is introduced into the snowpack by either a rain event or the melt due to the incoming flux of shortwave radiation. In this moistening phase the LWC (yellow line) varies with a diurnal cycle. Repeated cycles of partial melting and refreezing conduce the snowpack to the isothermal state. During the ripening period, a combination of different situations can occur depending on the weather conditions but an increasing trend of the LWC is visible. Once the snowpack is isothermal and it cannot retain water anymore, it starts to produce water output until it melts totally. This last phase starts with a significant decrease of the SWE (red line).

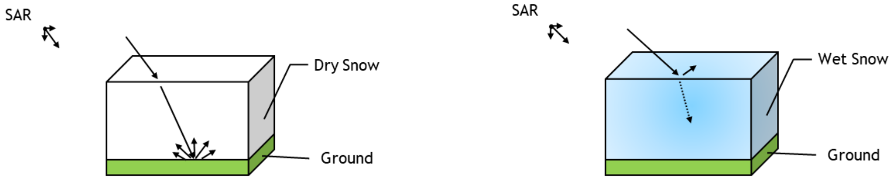

**Figure 2.** Main SAR backscattering mechanisms in presence of dry and wet snow at C-band. The dry snow is almost transparent, and the radar echo can penetrate the snow for several meters. The presence of LWC, causes high dielectric loss, which increases the absorption coefficient.

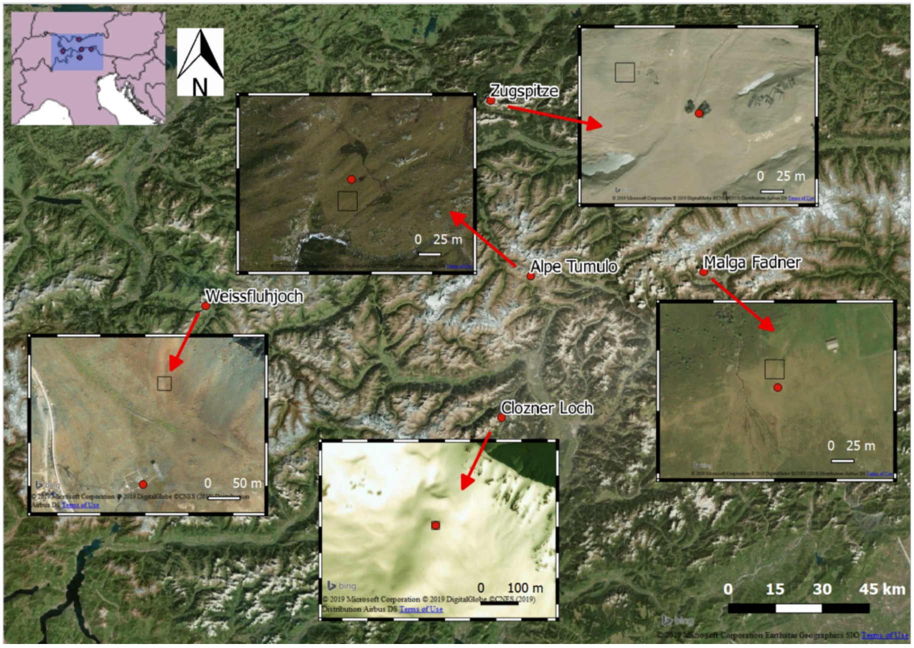

**Figure 3.** Overview map with the five stations used for the presented study (©2019 Microsoft Corporation ©2019 Digital Globe ©CNES(2019) Distribution Airbus DS). The red points indicate the exact location of the stations. The black squares indicate the S-1 footprints. The footprints were selected in order to minimize any possible interference of the EM wave with the homemade structures but maintaining a certain correlation with the in situ measurements. The panoramic images give an idea about the land cover type and the topography around the stations.

https://doi.org/10.5194/tc-2019-175
Preprint. Discussion started: 4 September 2019

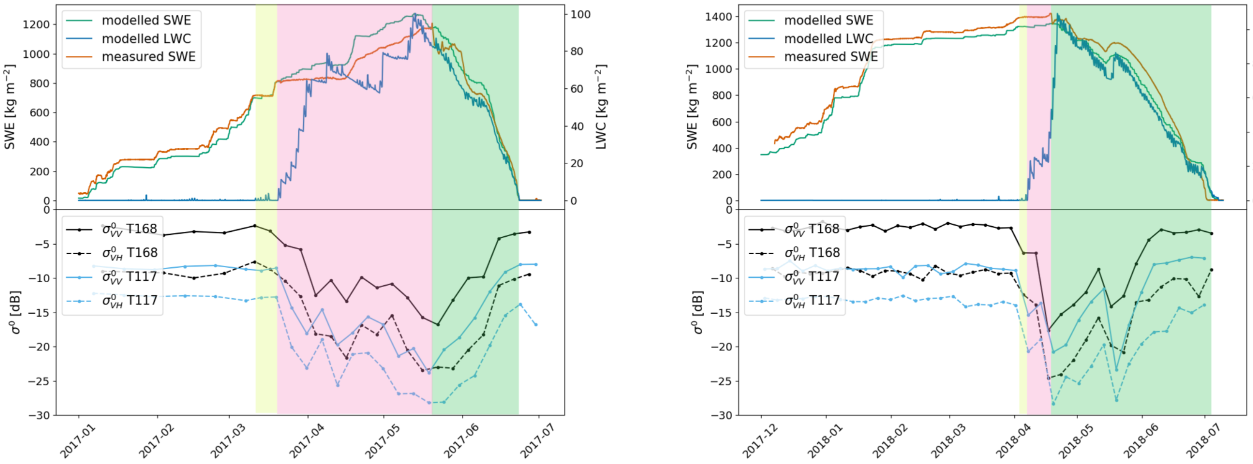

(a) Zugspitze, season 2016/2017

(b) Zugspitze, season 2017/2018

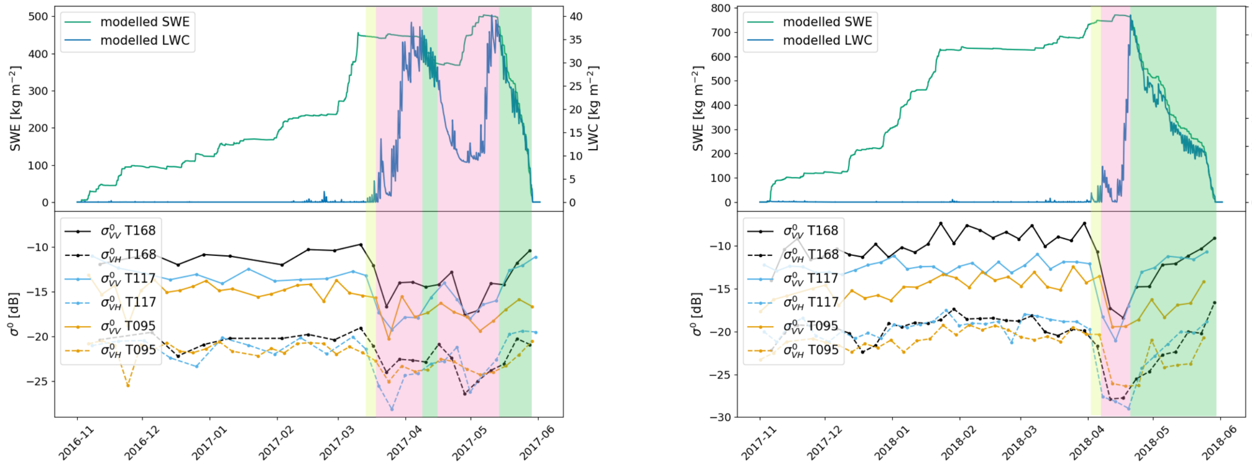

(c) Alpe del Tumulo, season 2016/2017

(d) Alpe del Tumulo, season 2017/2018

**Table 1.** Simplified SAR backscattering response to wet snow divided in volumetric, $\sigma^0_{vol}$, and surface backscattering, $\sigma^0_{sup}$, contributions. Considering a sufficiently thick snowpack the contribution of $\sigma^0_{grd}$ can be neglected.

| Parameter | $\sigma^0_{vol}$ | $\sigma^0_{sup}$ |
|---|---|---|
| Liquid water content (LWC) | negative correlation | positive correlation |
| Snow density (DS) | negative correlation | positive correlation |
| Snow grain size (GS) | positive correlation | - |
| Surface roughness (RS) | - | positive correlation |

https://doi.org/10.5194/tc-2019-175
Preprint. Discussion started: 4 September 2019

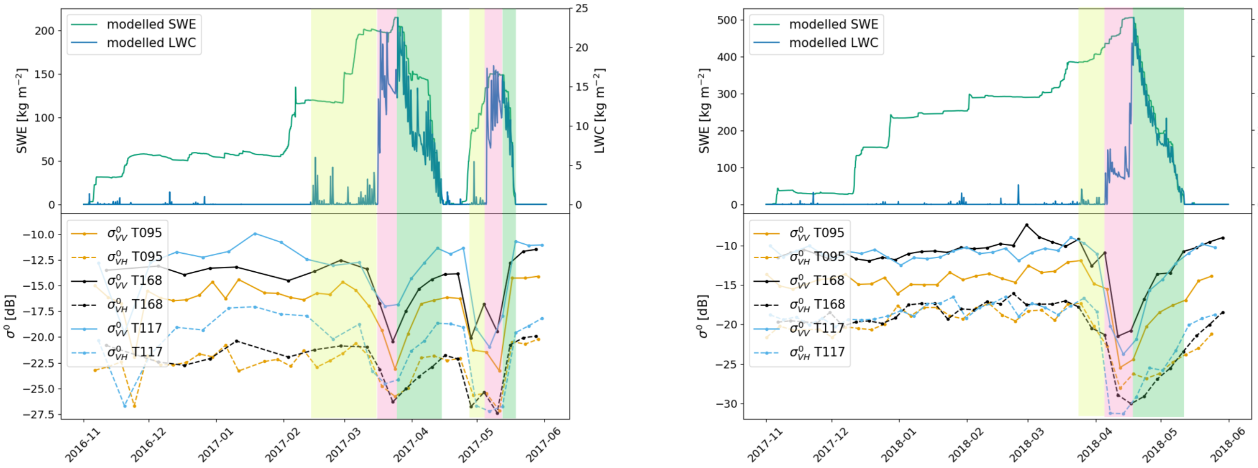

(e) Clozner Loch, season 2016/2017

(f) Clozner Loch, season 2017/2018

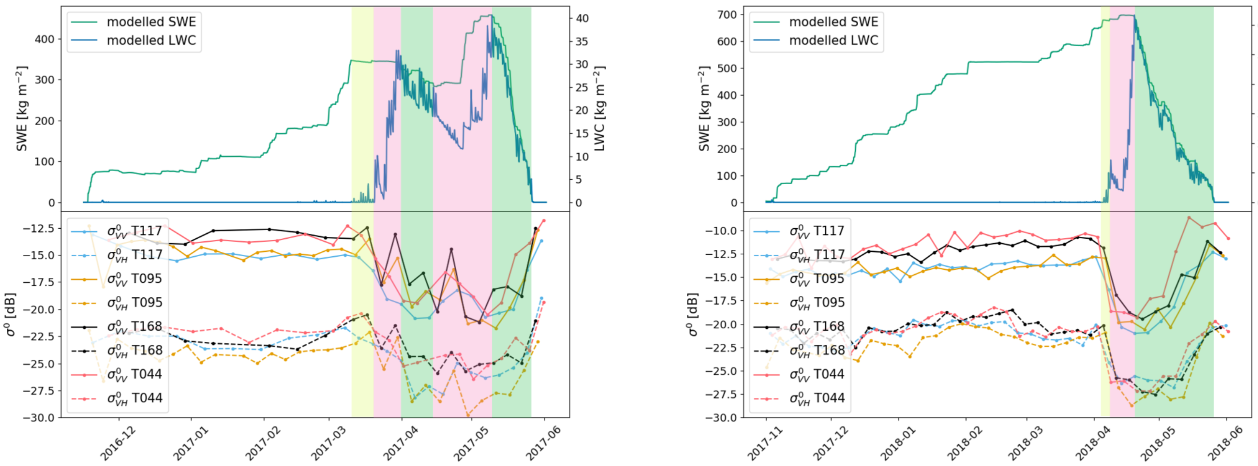

(g) Malga Fadner, season 2016/2017

(h) Malga Fadner, season 2017/2018

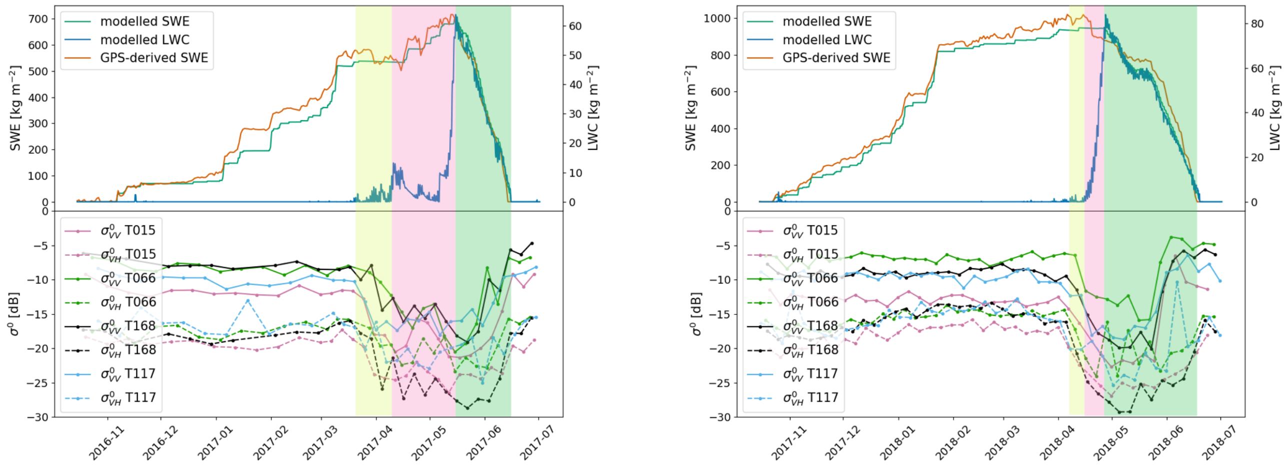

(i) Weissfluhjoch, season 2016/2017

(j) Weissfluhjoch, season 2017/2018

**Figure 4.** Temporal evolution of the coefficient of backscattering acquired over the five test sites compared to LWC and SWE measured in situ at the stations (when available) and modeled with SNOWPACK (contains modified Copernicus Sentinel data, 2016/2018, processed by Eurac Research). The three phases during the melting have been identified from the in situ/modeled data. The first phase of moistening is reported in light yellow, the ripening phase in light red and the runoff in light green. For all the test sites we found that the multi-temporal SAR measurements confirm the identification of the three melting phases. In detail, we systematically found that the SAR backscattering decreases as soon the snow starts containing water and increases as soon as SWE starts decreasing, which corresponds to the release of meltwater from the snowpack.

**Table 2.** Details of the meteorological and snow parameters measured at each station. Wind velocity (VW), wind direction (DW), air temperature (TA), relative humidity (RH), snow depth (HS), snow temperature at different depths (TS), surface temperature (TSS), soil temperature (TSG), incoming shortwave radiation (ISWR), incoming longwave radiation (ILWR), outgoing shortwave radiation (OSWR), snow water equivalent (SWE), snow density (DS), liquid water content (LWC) and ice content (IC).

| Station | Latitude, Longitude | Altitude [m a.s.l.] | Available measurements |
|---|---|---|---|
| Zugspitze (Germany) | 10.9835, 47.4064 | 2420 | VW, DW, TA, RH, HS, TSS, ISWR, OSWR, SWE, DS, LWC, IC |
| Alpe del Tumulo (Italy) | 11.1487, 46.9136 | 2230 | VW, DW, TA, RH, HS, TS, TSS, TSG, ISWR |
| Clozner Loch (Italy) | 11.0283, 46.5134 | 2165 | VW, DW, TA, RH, HS, TS, TSS, TSG, ISWR |
| Malga Fadner (Italy) | 11.8614, 46.9256 | 2155 | VW, DW, TA, RH, HS, TS, TSS, TSG, ISWR |
| Weissfluhjoch (Switzerland) | 9.8096, 46.8296 | 2455 | VW, DW, TA, RH, HS, TSS , TSG, ISWR, OSWR, SWE |

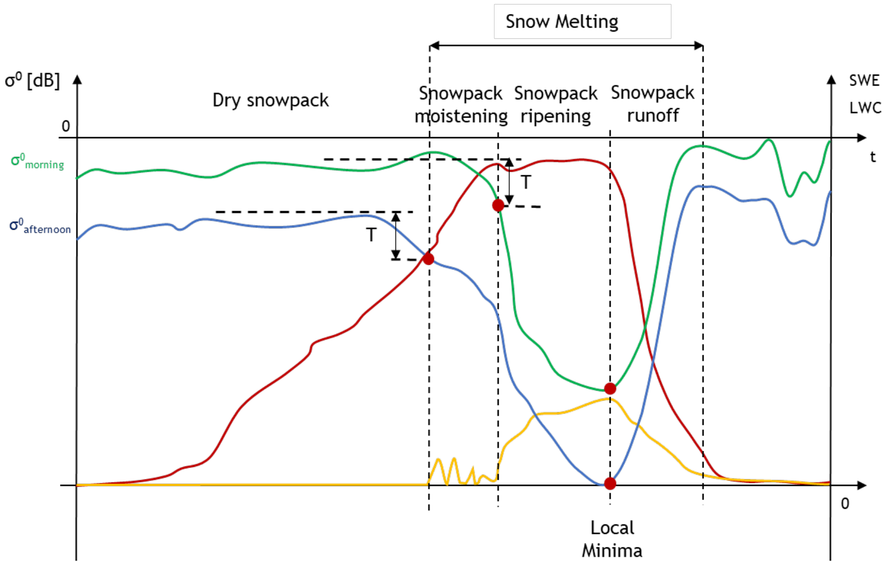

**Figure 5.** Schematic representation of the evolution of the backscattering coefficient acquired in the morning (green line) and in the afternoon (blue line) compared with LWC (yellow line) and SWE (red line) evolution. The offset between the morning and afternoon signals is due to the generally different local incidence angle of the ascending and descending acquisitions in mountainous regions. The three melting phases are identified from the LWC and SWE information. Correspondingly, the rules for the identification of each phase from the time series of $\sigma^0$ is highlighted: a decreases of at least T [dB] from the mean value in dry snow condition applied to the afternoon and morning signals identifies the moistening and ripening onsets respectively. The local minima of the signals indicate the runoff onset.

**Table 3.** SNOWPACK calibration results for each test site. Pearson correlation coefficient ($\rho$) and the mean absolute error (MAE) have been computed for snow depth (HS), snow temperatures at three different depth TS1 (0 m from the ground), TS2 (0.2 m from the ground), TS3 (0.5 m from the ground) and SWE, according to the availability of the ins situ data.

| | | Calibration results | | | | | | | | | |
|---|---|---|---|---|---|---|---|---|---|---|---|
| Station | Roughness [m] | HS | | TS1 | | TS2 | | TS3 | | SWE | |
| | | $\rho$ | MAE [cm] | $\rho$ | MAE [°C] | $\rho$ | MAE [°C] | $\rho$ | MAE [°C] | $\rho$ | MAE [$\mathrm{kgm}^{-2}$] |
| Zugspitze | 0.005 | 0.99 | 3.7 | - | - | - | - | - | - | 0.99 | 47.8 |
| Alpe Tumulo | 0.03 | 0.99 | 3.6 | 0.90 | 0.4 | 0.93 | 0.4 | 0.88 | 0.5 | - | - |
| Clozner Loch | 0.01 | 0.99 | 4.1 | 0.87 | 0.8 | 0.78 | 1.8 | - | - | - | - |
| Malga Fadner | 0.01 | 0.99 | 2.8 | 0.83 | 0.6 | 0.83 | 0.7 | 0.85 | 1.2 | - | - |
| Weissfluhjoch | 0.002 | 0.99 | 2.8 | - | - | - | - | - | - | 0.99 | 35.1 |

https://doi.org/10.5194/tc-2019-175
Preprint. Discussion started: 4 September 2019

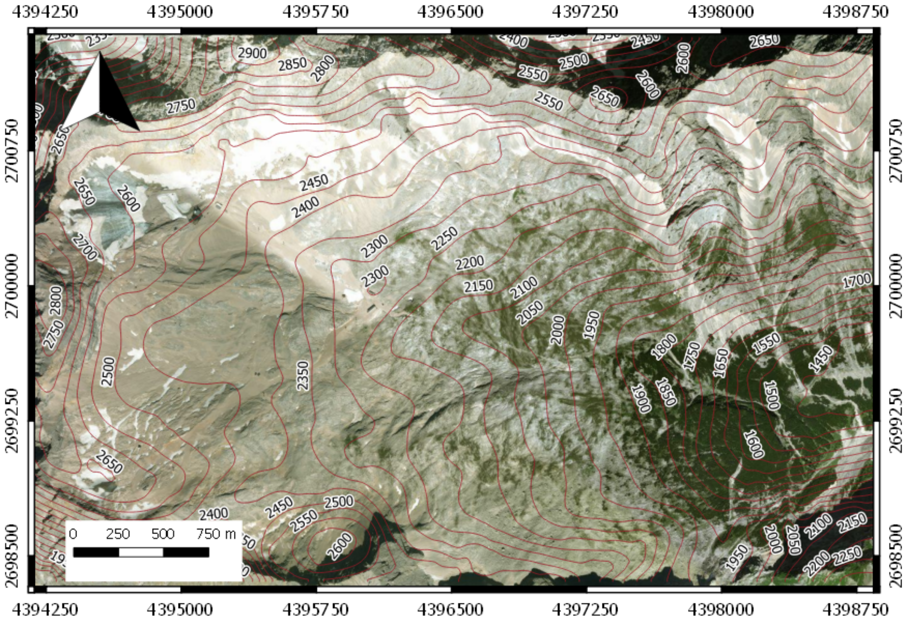

(a)

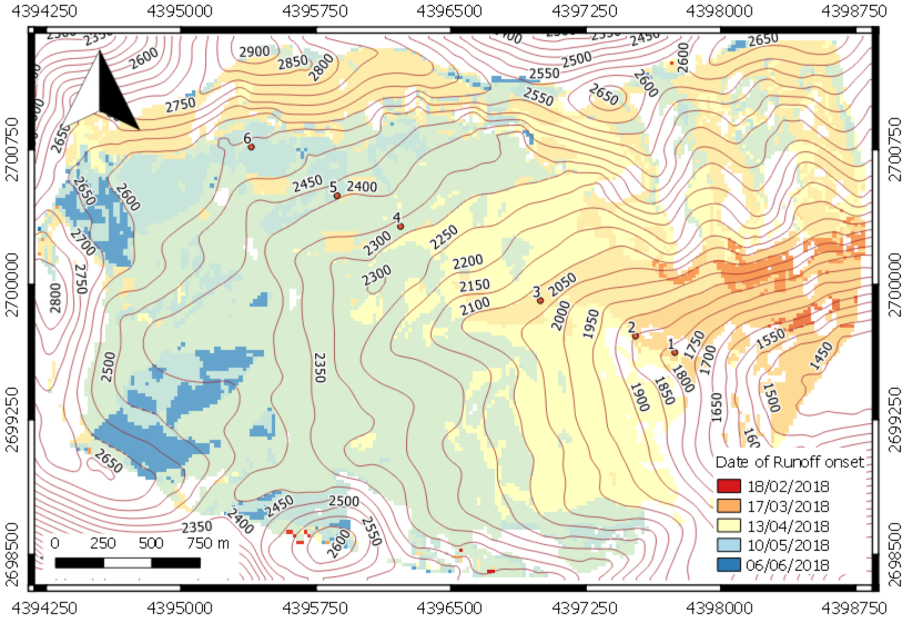

(b)

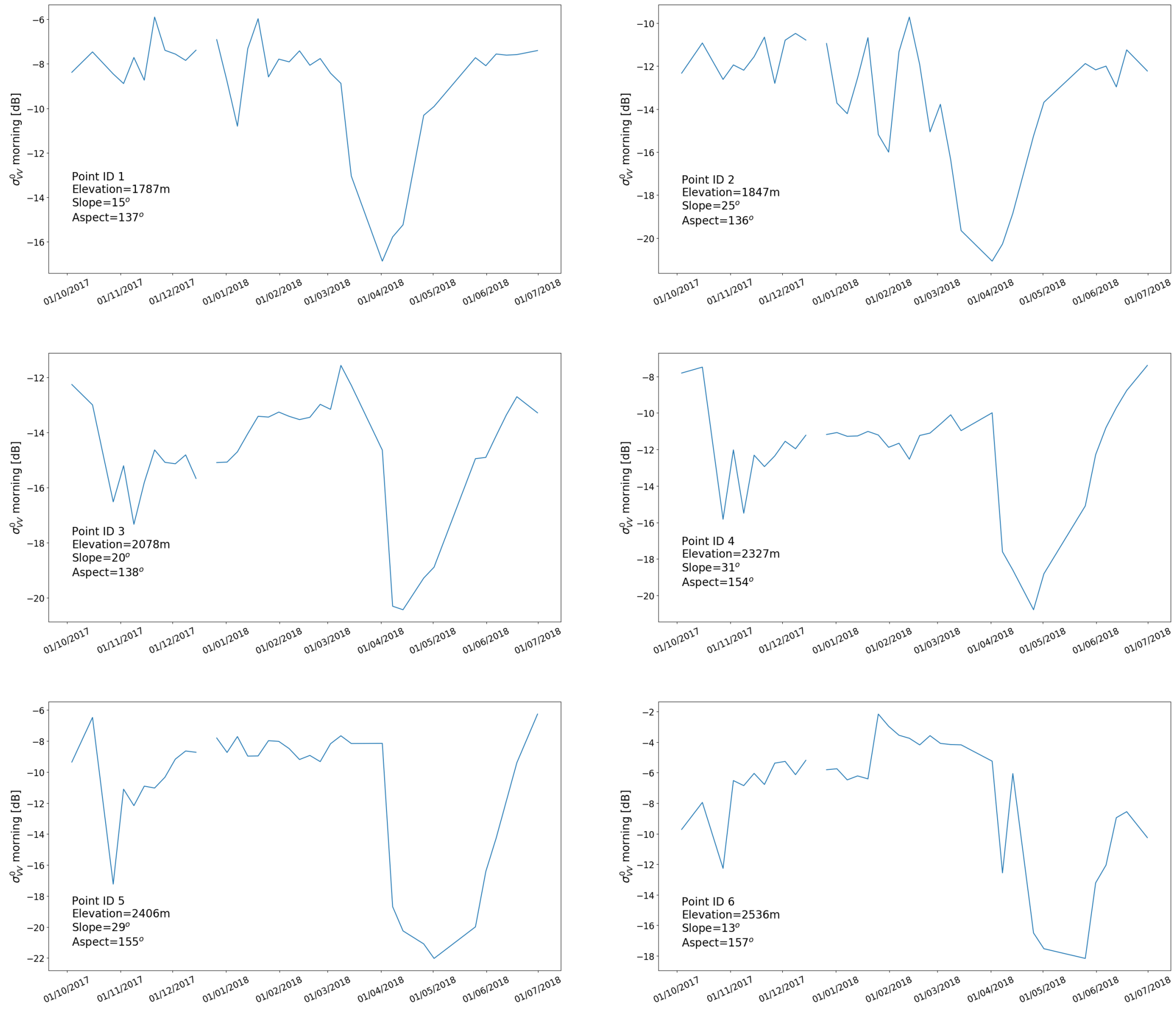

(c)

**Figure 6.** Run-off onset for the Zugspitzplatt catchment. (a) Test site presentation (©2019 Microsoft Corporation ©2019 Digital Globe ©CNES(2019) Distribution Airbus DS) (b) Map of the run-off onset (contains modified Copernicus Sentinel data, 2018, processed by Eurac Research). The run-off started at lower altitude and at the south exposed slopes. The last areas to have the runoff in the catchment are the high-altitude area, the north exposed and glacierized areas. (c) The multitemporal backscattering time series for the selected points identified in (b). All the time series present the characteristic “U-shaped” pattern.

https://doi.org/10.5194/tc-2019-175
Preprint. Discussion started: 4 September 2019

**Table 4.** List of the Sentinel-1 acquisitions and their main characteristics over the five test sites.

| Test Site | Relative orbit number (i.e., track number) | Time of the acquisition | Orbit Direction | Local incidence angle (LIA) |
|---|---|---|---|---|
| Zugspitze | 117 | Afternoon | Ascending | 38° |
| | 168 | Morning | Descending | 39° |
| Alpe Tumulo | 095 | Morning | Descending | 47° |
| | 117 | Afternoon | Ascending | 35° |
| | 168 | Morning | Descending | 40° |
| Clozner Loch | 095 | Morning | Descending | 43° |
| | 117 | Afternoon | Ascending | 39° |
| | 168 | Morning | Descending | 36° |
| Clozner Loch | 044 | Afternoon | Ascending | 34° |
| | 095 | Morning | Descending | 48° |
| | 117 | Afternoon | Ascending | 46° |
| | 168 | Morning | Descending | 38° |
| Weissfluhjoch | 015 | Afternoon | Ascending | 43° |
| | 066 | Morning | Descending | 31° |
| | 117 | Afternoon | Ascending | 33° |
| | 168 | Morning | Descending | 41° |

| | S-1 | Reference | Difference [days] |
|---|---|---|---|
| Moistening | - | 11/03/2017 | - |
| Ripening | 23/03/2017 | 21/03/2017 | +2 |
| Run-off | 20/05/2017 | 20/05/2017 | 0 |

(a) Zugspitze, season 2016/2017

| | S-1 | Reference | Difference [days] |
|---|---|---|---|
| Moistening | - | 04/04/2018 | - |
| Ripening | 05/04/2018 | 08/04/2018 | -3 |
| Run-off | 18/04/2018 | 18/04/2018 | 0 |

(b) Zugspitze, season 2017/2018

| | S-1 | Reference | Difference [days] |
|---|---|---|---|
| Moistening | 19/03/2017 | 14/03/2017 | +5 |
| Ripening | 23/03/2017 | 20/03/2017 | +3 |
| Run-off 1 | 24/03/2017 | 08/04/2017 | -14 |
| Run-off 1 | 01/05/2017 | 13/05/2017 | -13 |

(c) Alpe del Tumulo, season 2016/2017

| | S-1 | Reference | Difference [days] |
|---|---|---|---|
| Moistening | 07/04/2018 | 02/04/2018 | +5 |
| Ripening | 11/04/2018 | 07/04/2018 | +4 |
| Run-off | 14/04/2018 | 20/04/2018 | -6 |

(d) Alpe del Tumulo, season 2017/2018

| | S-1 | Reference | Difference [days] |
|---|---|---|---|
| Moistening 1 | 23/02/2017 | 14/02/2017 | +9 |
| Moistening 2 | - | 29/04/2017 | - |
| Ripening 1 | 12/03/2017 | 16/03/2017 | -4 |
| Ripening 2 | 28/04/2017 | 05/05/2017 | -7 |
| Run-off 1 | 22/03/2017 | 25/03/2017 | -3 |
| Run-off 2 | 08/05/2017 | 13/05/2017 | -5 |

(e) Clozner Loch, season 2016/2017

| | S-1 | Reference | Difference [days] |
|---|---|---|---|
| Moistening | - | 25/03/2018 | - |
| Ripening | - | 06/04/2018 | - |
| Run-off | 12/04/2018 | 18/04/2018 | -6 |

(f) Clozner Loch, season 2017/2018

| | S-1 | Reference | Difference [days] |
|---|---|---|---|
| Moistening | 19/03/2017 | 14/03/2017 | +5 |
| Ripening | 23/03/2017 | 20/03/2017 | +3 |
| Run-off 1 | 10/04/2017 | 30/03/2017 | +11 |
| Run-off 2 | 07/05/2017 | 09/05/2017 | -2 |

(g) Malga Fadner, season 2016/2017

| | S-1 | Reference | Difference [days] |
|---|---|---|---|
| Moistening | 07/04/2018 | 05/04/2018 | +2 |
| Ripening | 11/04/2018 | 07/04/2018 | +4 |
| Run-off | 21/04/2018 | 19/04/2018 | +2 |

(h) Malga Fadner, season 2017/2018

| | S-1 | Reference | Difference [days] |
|---|---|---|---|
| Moistening | 25/03/2017 | 19/03/2017 | +6 |
| Ripening | 04/04/2017 | 09/04/2017 | -5 |
| Run-off | 14/05/2017 | 16/05/2017 | -2 |

(i) Weissfluhjoch, season 2016/2017

| | S-1 | Reference | Difference [days] |
|---|---|---|---|
| Moistening | 06/04/2018 | 02/04/2018 | +4 |
| Ripening | 10/04/2018 | 17/04/2018 | -7 |
| Run-off | 08/05/2018 | 19/04/2018 | +19 |

(j) Weissfluhjoch, season 2017/2018

**Table 5.** Onset times for the melt phases identified in the five test sites using the LWC and SWE (reference) and Sentinel-1 with the method proposed in the previous section.